Petroleum 12 (2026) 216–229

Contents lists available at ScienceDirect

Petroleum

journal homepage: www.keaipublishing.com/en/journals/petlm

Full Length Article

Structural evolution and reservoir-control mechanisms of ultra-deep strike–slip fault zones in the Fuman area, Tarim Basin, China

Peng Cao [a,b,c], Xiongqi Pang [a,b,*], Jiajun Chen [d], Shaoying Chang [d], Jorge Costa Gomes [c]

[a] State Key Laboratory of Petroleum Resources and Engineering, China University of Petroleum (Beijing), Beijing, 102249, China
[b] College of Geosciences, China University of Petroleum (Beijing), Beijing, 102249, China
[c] CNPC R&D Company Limited, Dubai, United Arab Emirates
[d] Hangzhou Research Institute of Geology, PetroChina, Hangzhou, 310023, China

ARTICLE INFO

Article history:
Received 30 October 2025
Received in revised form
19 March 2026
Accepted 7 April 2026

Keywords:
Strike–slip fault
Slip intensity
Fault-controlled reservoir
Ultra-deep carbonate
Fuman oilfield
Tarim Basin

ABSTRACT

The discovery of ultra-deep strike–slip fault–controlled hydrocarbon reservoirs in the central Tarim Basin has renewed interest in the structural evolution and reservoir-controlling mechanisms of intracratonic strike–slip systems. Based on integrated drilling data, high-resolution 3D seismic reflection interpretation, and structural analog modeling, this study investigates the F_I12 and F_I17 fault zones in the Fuman area as representative examples. The results show that ultra-deep strike–slip faults exhibit combined lateral segmented growth and vertical stratified propagation, with secondary shear faults overlapping and stepping in both horizontal and vertical directions. To characterize fault activity in a reproducible manner, a semi-quantitative slip intensity framework is established using fault-zone width, structural relief, and segmentation complexity. Comparative analysis demonstrates that slip intensity is the first-order control on the scale and effectiveness of fault-controlled carbonate reservoirs: fault zones with higher slip intensity develop wider damage zones, stronger fracture connectivity, and larger reservoir volumes. Within individual fault zones, slip intensity is preferentially concentrated at lateral step-overs and relay zones of secondary shear faults, where large-scale fracture corridors form and hydrocarbon productivity is significantly enhanced. In addition, for reservoirs characterized by a lower-source–upper-reservoir configuration, hydrocarbon productivity is positively correlated with the proximity of vertical fault step-overs to the target reservoir interval. Shallower vertical overlap facilitates more efficient upward hydrocarbon migration, resulting in higher hydrocarbon abundance. These results establish a three-dimensional structural control model linking slip intensity, fault architecture, and reservoir effectiveness in ultra-deep carbonate strike–slip systems, providing a robust geological basis for reservoir prediction and exploration risk reduction in complex ultra-deep settings.

© 2026 Southwest Petroleum University. Publishing services by Elsevier B.V. on behalf of KeAi Communications Co. Ltd. This is an open access article under the CC BY-NC-ND license (http://creativecommons.org/licenses/by-nc-nd/4.0/).

1. Introduction

The Fuman Oilfield, located in the central Tarim Basin, represents the core exploration province for ultra-deep carbonate hydrocarbons in China. Ordovician carbonate reservoirs in this area are commonly buried at depths exceeding 6000 m and locally deeper than 8000 m, see Fig. 1(a), defining a typical ultra-deep hydrocarbon system with complex structural conditions. With the global focus of petroleum exploration progressively shifting toward deep and ultra-deep targets, such resources have become increasingly important for long-term energy supply security. However, prolonged burial and multistage diagenetic modification have resulted in severely degraded primary reservoir properties. Average porosity is generally lower than 4%, and permeability is commonly less than 1 mD, classifying these reservoirs as tight carbonate systems.

The stratigraphic succession of the Fuman Oilfield extends from the Neoproterozoic Nahua System to the Quaternary, with a total

* Corresponding author.
E-mail addresses: caopeng@cnpcrd.com (P. Cao), pangxq@cup.edu.cn (X. Pang).
Peer review under the responsibility of Southwest Petroleum University

https://doi.org/10.1016/j.petlm.2026.04.003
2405-6561/© 2026 Southwest Petroleum University. Publishing services by Elsevier B.V. on behalf of KeAi Communications Co. Ltd. This is an open access article under the CC BY-NC-ND license (http://creativecommons.org/licenses/by-nc-nd/4.0/).

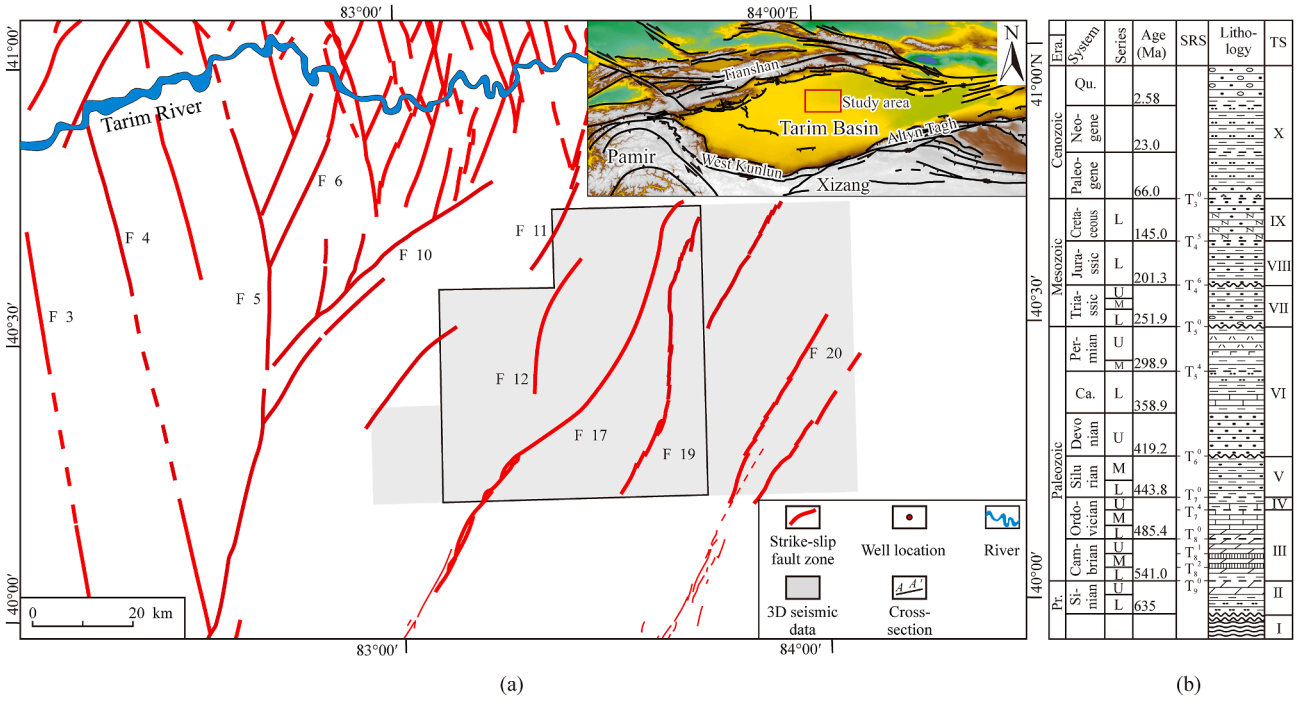

Fig. 1. Distribution map of F_i17 and F_i12 fault locations in the study area: (a) distribution of small-scale intracratonic strike-slip faults of the Lower Paleozoic tectono-stratigraphic (TS) unit in the northern Tarim Basin; (b) comprehensive stratigraphic column showing the abbreviationss of seismic reflection surfaces and ten TS units of the Tarim Basin (modified after [2]).

thickness of approximately 11 km shown in Fig. 1(b). The uppermost ~2400 m comprises Cenozoic strata (Quaternary, Neogene, and Paleogene), dominated by conglomerates, sandstones, and mudstones and characterized by multiple sedimentary cycles with an overall upward-coarsening trend. The Mesozoic succession (~1400 m thick) includes Triassic, Lower Jurassic, and Lower Cretaceous strata, mainly composed of sandstones and mudstones, with the Triassic interval dominated by mudstones and lithic sandstones and the Lower Cretaceous characterized by feldspar-rich sandstones in the lower part and lithic-rich sandstones upward. The Upper Paleozoic sequence (1300–1400 m thick) consists of Permian igneous and clastic rocks, Carboniferous marine clastic rocks interbedded with limestone, and Upper Devonian sandstones and siltstones. In contrast, the Lower Paleozoic succession is dominated by extensive carbonate deposition from the Lower Cambrian to Middle Ordovician, accompanied by Middle Cambrian gypsiferous rocks, Upper Ordovician mudstones, and Silurian clastic rocks. Beneath these units, the Sinian (Ediacaran) strata consist of clastic rocks overlain by dolomite, while coarse clastic rocks of the Nahua System occur locally within Neoproterozoic rift settings. Overall, the stratigraphic framework of the study area can be subdivided into eleven tectonostratigraphic units based on regionally developed unconformities.

Under such conditions, strike–slip faults generated by strong intracontinental tectonic activity play a first-order role in reservoir formation. Brittle deformation associated with strike–slip faulting creates dense fracture networks, while fault-related fluid circulation promotes dissolution, recrystallization, and brecciation, collectively forming high-quality secondary pore spaces. As a result, understanding the reservoir-controlling mechanisms of strike–slip faults has become a key challenge for overcoming exploration bottlenecks in ultra-deep carbonate settings. Exploration practice in the Fuman Oilfield demonstrates that hydrocarbon discoveries and well productivity are strongly dependent on the development degree and internal architecture of strike–slip fault zones. Observations from fault damage zones, including core and outcrop analogs, reveal widespread fractures and breccias, where porosity can increase to 8–15% and permeability may be enhanced by two to three orders of magnitude compared with adjacent host rocks, forming localized sweet spots favorable for hydrocarbon accumulation.

Despite their favorable reservoir effects, ultra-deep strike–slip fault systems are characterized by pronounced structural complexity, which poses significant challenges for exploration and development. Strong fault segmentation leads to substantial lateral variations in reservoir quality along individual fault zones. In addition, Cambrian–Ordovician carbonate successions in the Fuman area have experienced multiple tectonic episodes, including the Caledonian, Hercynian, Indosinian, Yanshanian, and Himalayan orogenies [1], resulting in superimposed deformation styles and extreme reservoir heterogeneity. These factors collectively contribute to large productivity differences among wells drilled in different structural positions, even within the same fault zone.

Recent advances in geology–engineering integration and whole petroleum system analysis emphasize the necessity of incorporating mechanical stratigraphy, structural architecture, and engineering constraints into the evaluation of ultra-deep reservoirs [2–4]. These studies provide an important conceptual foundation for fault-controlled carbonate reservoirs and support integrated approaches that link fault evolution with reservoir performance. Meanwhile, extensive studies have investigated the geometry and kinematics of strike–slip faults using 3D seismic interpretation [5–7], sandbox physical modeling [8], and numerical simulation [9]. These works have clarified fault growth processes, segmentation patterns, and large-scale structural controls on reservoir modification. Classical strike–slip fault models [10], damage-zone theories [11,12], and experimentally derived fault propagation concepts [13] further establish the theoretical framework for understanding fault-related deformation.

Nevertheless, most existing studies focus primarily on fault geometry and kinematic evolution, while the quantitative or semi-quantitative linkage between fault deformation characteristics and differential reservoir-controlling effects remains insufficiently constrained. In particular, the lack of an explicit framework to describe variations in fault activity hampers the interpretation of productivity differences between wells and limits predictive capability at the field scale.

To address these issues, this study integrates deep drilling data, high-resolution seismic reflection profiles, and production performance records, focusing on the F_I12 and F_I17 strike–slip fault zones in the Fuman Oilfield as Fig. 1(a). A semi-quantitative slip intensity framework is established based on fault-zone width, displacement hierarchy, and structural complexity, and its relationship with reservoir development and well productivity is systematically evaluated. The objectives of this study are to: (1) characterize the structural architecture and evolutionary styles of ultra-deep strike–slip fault zones; (2) clarify the differential reservoir-controlling mechanisms associated with variations in slip intensity; and (3) demonstrate a reproducible workflow for fault-controlled reservoir prediction in ultra-deep carbonate systems. The results provide new insights into strike–slip fault–reservoir coupling and offer practical guidance for exploration and development in ultra-deep settings.

2. Geological setting

The Tarim Basin is a large, superimposed cratonic basin underlain by a Precambrian crystalline basement formed during the breakup of the Neoproterozoic Rodinia supercontinent. Since the Paleozoic, the basin has experienced multiple phases of tectonic reactivation, resulting in a complex composite sedimentary and structural framework [14–17]. The Fuman Oilfield is located in the central Tarim Basin, bounded by the Tazhong Uplift to the south, the Tabei Uplift to the north, the Manjiaer Depression to the east, and the Awati Depression to the west. Structurally, the area forms a saddle-shaped paleohigh as Fig.1(a) that has remained relatively stable over long geological timescales, providing favorable conditions for hydrocarbon accumulation.

Recent studies on the Tarim Basin have provided important constraints on shoal-facies carbonate development, multistage tectonic evolution, strike–slip fault systems (including the F_I17 and F_I19 fault zones in the Fuman area), karstification processes, and regional thermal history [18–23]. These results form the geological basis for interpreting the timing of strike–slip fault reactivation and its coupling with carbonate reservoir enrichment in the study area.

The stratigraphic succession in the Fuman Oilfield ranges from the Cenozoic to the Paleozoic as Fig. 1(b), including Cenozoic Quaternary and Neogene strata; Mesozoic Cretaceous, Jurassic, and Triassic units; and Paleozoic Permian, Carboniferous, Devonian, Silurian, and Ordovician formations. Cambrian and Sinian strata have not yet been fully penetrated by drilling. The primary exploration targets are Ordovician carbonate formations, which can be subdivided into the upper Sangtamu, Lianglitage, and Tumuxiuke formations; the middle Yijianfang Formation; and the middle–lower Yingshan Formation. Among these, the Yijianfang and Yingshan formations constitute the main hydrocarbon-bearing reservoirs.

From a mechanical stratigraphy perspective, the deep stratigraphic column in the Fuman area consists of alternating competent (brittle) and incompetent (ductile) layers, which exert a first-order control on the vertical segmentation and propagation of strike–slip faults [2]. From bottom to top, Sinian to Lower Cambrian strata are dominated by sandstones (Sinian only), limestones, and dolostones, forming a mechanically competent unit. The Middle Cambrian is characterized by interbedded gypsum, anhydrite-bearing dolostone, and dolostone, representing a relatively ductile layer. The Upper Cambrian to Middle Ordovician interval, with a thickness of approximately 2000–3000 m, consists mainly of dolostone in the lower part and limestone in the upper part and forms another mechanically competent unit. The Upper Ordovician Sangtamu Formation is composed predominantly of thick mudstone with thin argillaceous limestone interbeds and represents a weak layer with thicknesses ranging from 700 to 1700 m. Silurian to Carboniferous strata comprise alternating mudstone, siltstone, and fine sandstone with minor limestone interbeds, forming a mechanically heterogeneous interval. The Permian succession is dominated by basaltic and andesitic volcanic rocks and constitutes a strong and competent unit.

Strike–slip fault development exhibits pronounced vertical stratification in response to this mechanical layering. The F_I12 fault zone is mainly developed within the Cambrian to Middle Ordovician formations, while potential deeper extensions below the Cambrian cannot be clearly resolved using current seismic data (Figs. 2 and 3). In contrast, the F_I17 fault zone displays right-stepping en echelon normal faults within the Upper Ordovician–Carboniferous interval and minor extensional faults in the Triassic–Jurassic strata, indicating multiphase deformation and upward propagation through mechanically distinct layers [2,24].

Tectonically, ultra-deep strike–slip fault zones in the Tarim craton have experienced several major deformation stages, including Caledonian Stage I, Caledonian Stage III, Late Caledonian–Early Hercynian, and Late Hercynian events. These tectonic phases are recorded by regional unconformities developed at the tops of the Middle Ordovician, Upper Ordovician, Middle Silurian–Middle Devonian, and Permian strata, respectively [25]. The superposition of these deformation events provides the structural foundation for the complex architecture and variable slip intensity observed in the strike–slip fault zones of the Fuman Oilfield.

3. Research methodology

3.1. Integrated Seismic–Geological fault analysis

A comprehensive seismic–geological workflow was applied to characterize typical ultra-deep strike–slip fault zones in the Fuman Oilfield, integrating high-resolution 3D seismic reflection data, deep drilling information, and constrained structural interpretation. The analysis focuses on quantifying fault-zone geometry and internal architecture, which form the basis for evaluating variations in strike–slip fault slip intensity. Key parameters extracted from seismic data include fault-zone width, vertical structural relief, segmentation style, and displacement hierarchy. Structural contour maps were constructed for representative stratigraphic horizons, such as the top of the Yijianfang Formation, to constrain fault geometry and kinematics at reservoir depth.

To ensure the reliability and reproducibility of the interpretation, all seismic and well datasets were subjected to systematic quality control and uncertainty assessment. The 3D seismic volume was processed using band-pass filtering to preserve an effective frequency range of 20–50 Hz, with dominant frequencies of approximately 40–50 Hz within the target intervals. Based on interval velocities of 4000–6000 m/s, this corresponds to a vertical resolution of approximately 2–3 m according to the $\lambda/4$ criterion. Well–seismic calibration was performed using synthetic seismograms generated from sonic and density logs, yielding root-mean-square misties of 4–8 ms. After depth conversion, this translates to an estimated horizon-picking uncertainty of $\pm$10–20 m.

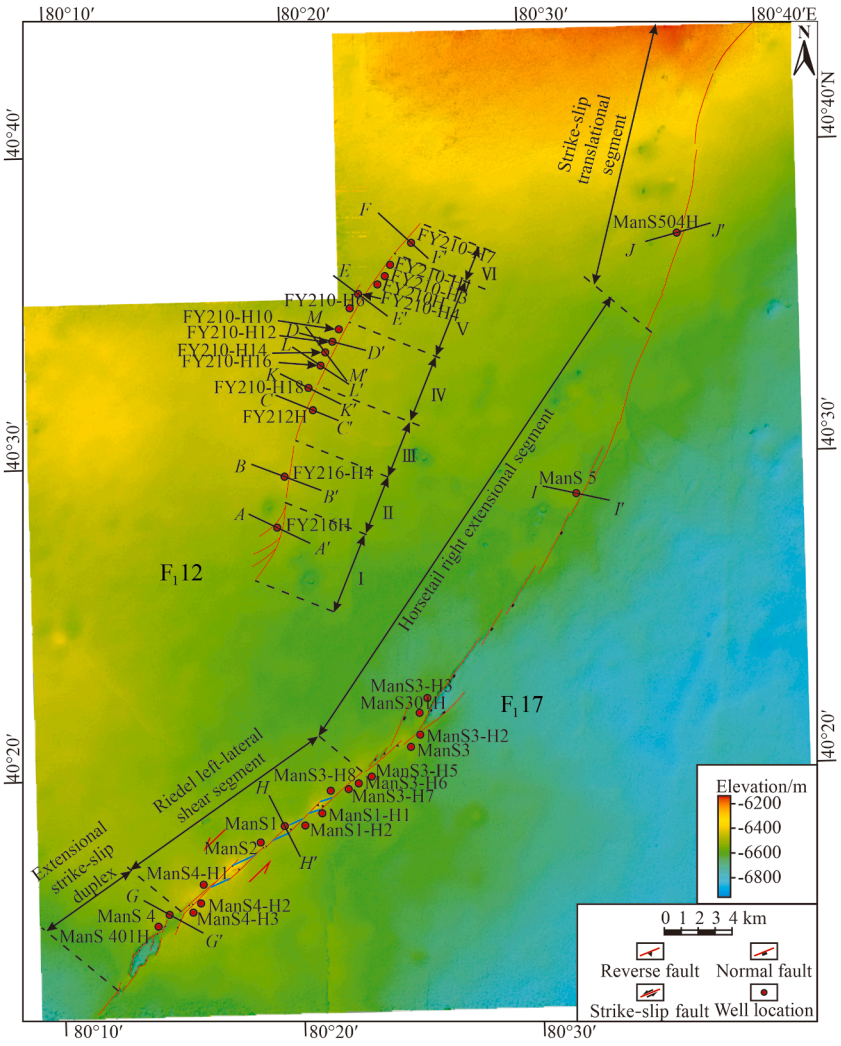

Fig. 2. Structural outline map of the top of the Yijianfang Formation for the $F_1$12 and $F_1$17 fault zones.

Fault positions and fault-zone widths were evaluated through repeated interpretations conducted independently by five interpreters. In addition, horizon picks were perturbed within the defined uncertainty ranges to assess the sensitivity of fault geometry to interpretation variability. The resulting depth and width uncertainties were subsequently propagated into structural modeling using a Monte Carlo sampling approach. Seismic horizon depths, fault geometries, and associated petrophysical parameters were sampled from Gaussian distributions defined by the interpreted uncertainty bounds. The influence of these uncertainties on derived permeability trends and productivity indicators is expressed as 95% confidence intervals in the subsequent analysis (section 5).

By explicitly incorporating interpretational uncertainty throughout the seismic–geological workflow, this methodology enhances the robustness of fault characterization and provides a reliable foundation for linking strike–slip fault architecture and slip intensity to differential reservoir development.

3.2. Structural physical modeling

Structural physical modeling, also referred to as analog modeling, is widely used in structural geology to reproduce and analyze deformation processes, kinematic evolution, and structural architectures observed in nature. When properly designed, analog experiments provide valuable insights into fault growth patterns and segmentation styles that cannot be directly observed at depth. The validity of analog modeling relies on the fulfillment of similarity principles between the model and the natural prototype, including geometric, kinematic, temporal, and dynamic similarity [26].

Geometric similarity requires that the dimensions of the physical model are appropriately scaled to represent natural structures while maintaining experimental feasibility. In practice, model dimensions are typically constrained between 100 and 1000 mm, corresponding to geometric scaling ratios (CL) on the order of 1×10^4 to 1.5×10^7. These scaling relationships ensure that the resulting deformation patterns are geometrically comparable to natural strike–slip fault systems.

Material similarity is essential for reproducing realistic deformation behavior. Natural rocks exhibit elastic, plastic, and brittle responses depending on stress conditions and lithology. Therefore, modeling materials must approximate not only the mechanical properties of rocks but also the mechanical contrasts between stratigraphic units. Factors such as internal friction, cohesion, density, and relative competence contrasts are considered to ensure that the model captures key aspects of fault initiation, propagation, and segmentation.

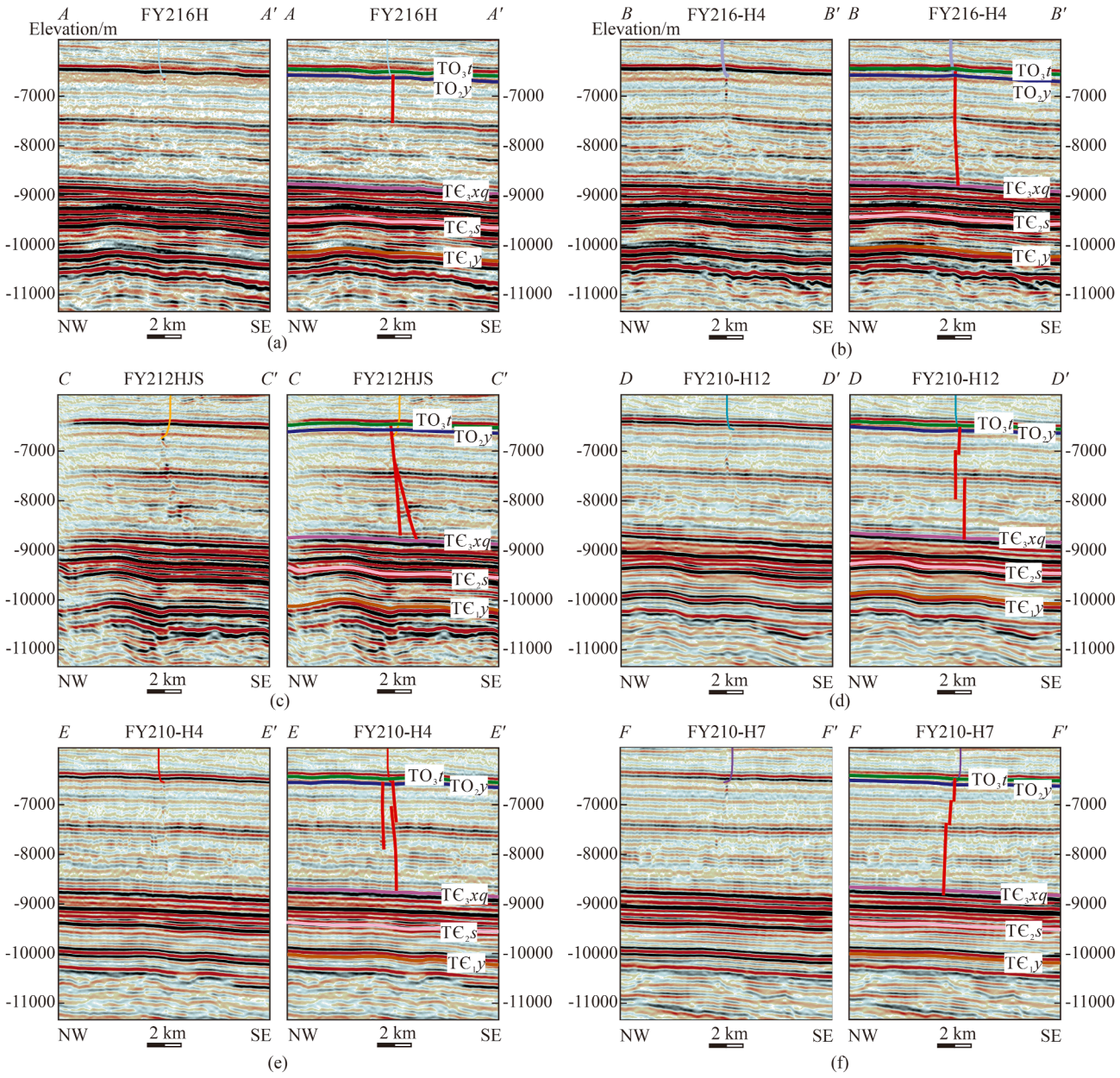

Fig. 3. Cross-sectional characteristics of each segment of the F_I12 fault zone: (a) segment I: seismic cross-section along the FY216H well trajectory; (b) segment II: seismic cross-section along the FY216–H4 well trajectory; (c) segment III: seismic cross-section along the FY212HJS well trajectory; (d) segment IV: Seismic cross-section along the FY210–H12 well trajectory; (e) segment V: Seismic cross-section along the FY210–H4 well trajectory; (f) segment VI: seismic cross-section along the FY210–H7 well trajectory.

Temporal similarity describes the proportional relationship between experimental time and geological deformation time. Typical temporal scaling ratios (Ct) range from approximately 2.1×10^4 to 6.8×10^9, implying that 1 h of experimental deformation corresponds to thousands to hundreds of thousands of years of natural tectonic evolution. Most experiments are conducted over minutes to hours, which is sufficient to capture the progressive development of fault zones under controlled boundary conditions.

Dynamic similarity ensures that applied boundary forces, including horizontal shear, vertical loading, and gravitational stress, produce deformation patterns analogous to those generated by natural tectonic processes. In analog experiments, the magnitude, orientation, and evolution of applied stresses are carefully controlled to reproduce strike–slip deformation regimes relevant to intracratonic settings.

In this study, dry quartz sand was selected as the primary modeling material to simulate brittle deformation associated with strike–slip faulting. Quartz sand exhibits frictional behavior comparable to that of brittle upper-crustal rocks and is well suited for reproducing fault localization and segmentation. In natural systems, sandstones typically display Young's moduli of approximately 3×10^4 MPa, Poisson's ratios around 0.25, internal friction angles near 30°, cohesions of ~10 MPa, and densities of ~2.6 g/cm^3. Carbonate rocks, represented by dense limestones, generally exhibit higher stiffness, with Young's moduli of approximately 6×10^4 MPa, similar Poisson's ratios and friction angles, higher cohesion (~17 MPa), and

densities of ~2.8 g/cm^3. These mechanical contrasts were incorporated conceptually into the model design to reproduce stratigraphic competence variations.

It should be emphasized that the physical modeling conducted in this study is used to qualitatively constrain fault growth styles, segmentation patterns, and vertical propagation behavior of strike–slip fault zones. The experiments are not intended to directly quantify fault slip or slip intensity. Instead, they provide structural context that supports the interpretation of seismic-derived fault architectures and the subsequent semi-quantitative evaluation of slip intensity based on fault-zone width, displacement hierarchy, and structural complexity.

4. Fault characteristics in the Fuman Oilfield, Tarim basin, NW China

4.1. Characteristics of the FI12 fault zone

The F_I12 fault zone is a first-order strike–slip fault system in the Fuman Oilfield, with an overall length of approximately 24 km. Vertically, the fault system extends downward into the Cambrian strata and locally propagates upward into the Ordovician Yingshan and Yijianfang formations (Fig. 2). Seismic interpretation reveals pronounced vertical segmentation and along-strike variability, reflecting the influence of long-term tectonic reactivation and strong mechanical stratification within the carbonate-dominated succession.

Based on vertical continuity, fault stacking patterns, and segmentation characteristics, the F_I12 fault zone can be subdivided into six segments (I–VI), each exhibiting distinct structural architectures (Fig. 2).

Segment I is characterized by a westward-diverging horsetail geometry in map view, indicative of distributed strike–slip deformation toward the fault termination. In cross section, see Fig. 3(a), minor subsidiary faults are developed within the upper Yingshan Formation and internally within the Yijianfang Formation, suggesting limited upward propagation.

Segment II consists of a single, laterally continuous fault displaying a clear strike–slip displacement style, with relatively simple internal structure, see Fig. 3(b).

Segment III contains two vertically stacked strike–slip faults developed within the Yingshan–Yijianfang interval and the Upper Cambrian–Penglaiba interval as Fig. 3(c), indicating vertical partitioning of deformation across mechanically distinct layers.

Segment IV shows three vertically superimposed strike–slip faults, distributed within the upper Yingshan–Yijianfang, Penglaiba–lower Yingshan, and Upper Cambrian–Penglaiba intervals as Fig. 3(d). This segment represents the most vertically complex architecture within the F_I12 fault zone.

Segment V comprises two vertically overlapping strike–slip faults located in the upper Yingshan–Yijianfang and Upper Cambrian–lower Yingshan strata as Fig. 3(e), reflecting partial vertical linkage of deformation.

Segment VI is characterized by three right-stepping, laterally offset strike–slip faults distributed across the Upper Cambrian–Penglaiba, lower Yingshan, and upper Yingshan–Yijianfang intervals as Fig. 3(f), forming a composite en echelon arrangement.

Overall, the F_I12 fault zone exhibits multi-level vertical segmentation combined with lateral linkage between fault segments. The prevalence of vertically stacked but only partially linked strike–slip faults suggests moderate cumulative slip and relatively weak vertical fault connectivity. This structural style reflects repeated reactivation under a mechanically layered stratigraphic framework and represents a fault zone with relatively low to moderate slip intensity compared with larger, more laterally continuous strike–slip systems in the Fuman area.

4.2. Characteristics of the FI17 fault zone

The F_I17 fault zone is another first-order strike–slip fault system in the Fuman Oilfield and represents the largest and most structurally complex fault zone in the study area. The fault zone has an overall map-view length of approximately 68 km and extends southward into an adjacent strike–slip fault system. The principal strike–slip fault cuts downward into the crystalline basement and locally propagates upward into the Ordovician Yijianfang Formation (Fig. 2), indicating strong vertical connectivity and long-term fault activity.

Based on cross-sectional structural styles and along-strike fault architectures, the F_I17 fault zone can be subdivided into four genetically distinct segments (Fig. 4): (1) an extensional strike–slip duplex segment, see Fig. 4(a); (2) a Riedel left-lateral shear segment, see Fig. 4(b); (3) a horsetail right-stepping extensional segment, see Fig. 4(c); and (4) a strike–slip translational segment, see Fig. 4(d) [24].

The extensional strike–slip duplex segment is characterized by a lozenge-shaped negative relief in plan view, indicative of a transtensional deformation regime. Seismic profiles reveal two boundary faults that define two relatively independent principal displacement zones (PDZ1 and PDZ2). Strata enclosed between the boundary faults are overall downthrown, forming a graben-like negative flower structure. This duplex structure is approximately 4 km long and 1 km wide, with a maximum vertical throw of up to 200 m. Within the lozenge-shaped graben, a series of nearly north–south–trending normal faults with small throws connect the two boundary faults. The left-stepping arrangement of the boundary faults indicates that this segment formed under left-lateral strike–slip motion, consistent with an extensional strike–slip duplex geometry.

The Riedel left-lateral shear segment extends for approximately 18 km along strike. In plan view, five lozenge-shaped positive relief structures are aligned along the principal displacement zone (PDZ2). In cross section, these uplifted zones are bounded by two major faults, with strata internally uplifted to form positive flower structures. The small angles between the boundary faults and the principal slip zone are characteristic of a classic R–P shear fracture system [10], where R and P represent synthetic and secondary synthetic shear fractures, respectively. Under left-lateral shear, right-stepping fault geometries generate localized compressional uplift, producing structurally favorable zones for fracture development.

The horsetail right-stepping extensional segment displays an arcuate plan-view geometry, with fault strikes gradually changing from approximately NE45° in the west to NE35° in the east, over a total length of about 30.2 km. In cross section, this segment is dominated by east-dipping transtensional faults developed mainly within the Cambrian to Middle Ordovician interval. Most adjacent transtensional faults show limited vertical overlap. Compared with the extensional duplex and Riedel shear segments to the southwest, fault throws in this segment are generally smaller (<80 m), indicating relatively weaker deformation intensity. On structural maps of the Silurian base, extensional normal faults are arranged in a right-stepping horsetail pattern, with fault strikes and lengths gradually diverging northward.

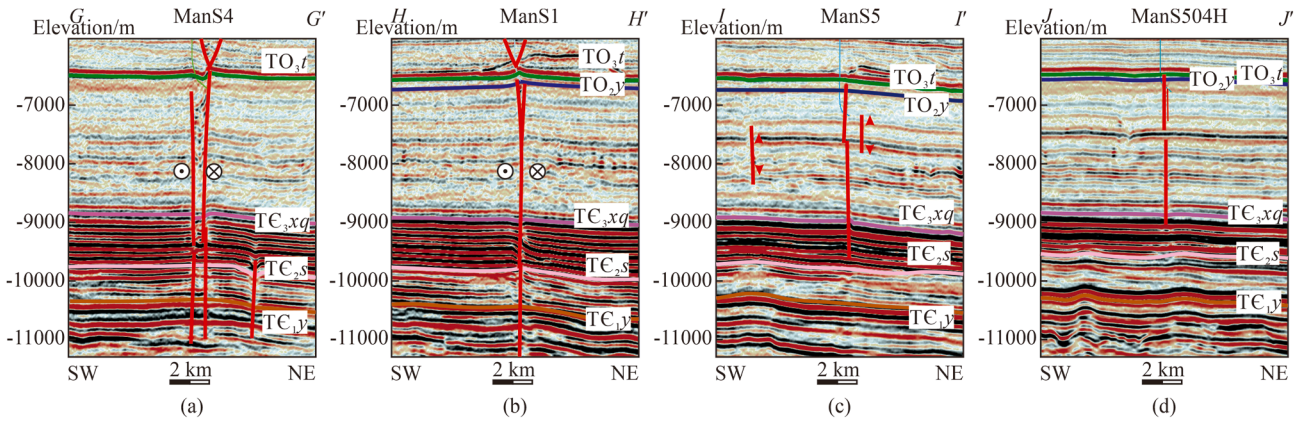

Fig. 4. Cross-sectional characteristics of each segment of the F_I17 fault zone: (a) extensional strike–slip duplex segment; (b) Riedel left-lateral shear segment; (c) horsetail right-stepping extensional segment; (d) strike–slip translational segment.

The strike–slip translational segment is located at the northern termination of the F_I17 fault zone and has a length of approximately 14.8 km. On seismic profiles, this segment is characterized by narrow, bead-like reflections with minimal structural relief. Deformation is mainly accommodated by two isolated, vertically developed strike–slip faults extending from the Upper Cambrian to the Middle Ordovician, which are connected by weak or soft linkage. This segment represents a zone of strain transfer rather than significant strain accumulation.

Overall, the F_I17 fault zone exhibits strong lateral continuity, well-developed segmentation, and complex combinations of extensional, compressional, and translational structural styles. The coexistence of large fault throws, wide damage zones, and laterally linked structural segments indicates high cumulative slip and strong slip intensity. Compared with the F_I12 fault zone, F_I17 represents a more mature and energetically active strike–slip system, providing a structural basis for enhanced fracture development and favorable fault-controlled reservoir formation.

5. Physical modeling of strike-slip fault development

To better constrain the development patterns and evolutionary sequences of strike–slip fault systems under shear deformation, three sets of comparative structural physical modeling experiments were designed. These experiments aim to investigate how fault architecture and segmentation styles vary with layer thickness and mechanical stratification, rather than to quantify fault slip or slip intensity directly. The three experimental configurations include: (1) a thin homogeneous material model; (2) a thick homogeneous material model; (3) a mechanically layered model composed of two superposed materials with contrasting properties.

5.1. Thin homogeneous material model (model 1)

In Model 1, 120-mesh dry quartz sand was used as the modeling material and placed between two rigid plastic plates. Thin marker layers of red sand were inserted at intervals of 1.5 cm, resulting in a total model thickness of 6 cm divided into four layers. The model dimensions were 50 cm in length and 24.5 cm in width. Deformation was imposed by single-sided left-lateral shear, with cumulative displacement increments of 11.8 mm, 23.4 mm, 25.2 mm, 36.5 mm, and 41.8 mm.

The evolution of the strike–slip fault zone can be divided into three main stages, see Fig. 5(a).

(1) Initial Riedel shear development stage, characterized by the formation of right-stepping echelon R shear fractures under left-lateral shear. Local uplift occurs at fracture step-overs, indicating localized compression.
(2) Progressive deformation stage, during which low-angle Y shear fractures develop preferentially at the step-over zones of the R shears.
(3) Fault linkage and maturation stage, marked by the development of secondary synthetic P shears and the linkage of Y shears to form a through-going fault surface subparallel to the principal displacement zone (PDZ).

This model illustrates the progressive organization of distributed shear fractures into a mature strike–slip fault zone under relatively uniform mechanical conditions.

5.2. Thick homogeneous material model (model 2)

Model 2 employed the same 120-mesh dry quartz sand but with a reduced total thickness of 4.5 cm, composed of three layers each 1.5 cm thick. The model geometry and boundary conditions were identical to Model 1, with single-sided left-lateral shear applied. Incremental displacement steps were 10.1 mm, 14.5 mm, 20.1 mm, and 26.1 mm.

The deformation process can also be subdivided into three stages as Fig. 5(b).

(1) An initial Riedel shear stage, with echelon R fractures and compressional uplift at step-overs.
(2) A secondary shear development stage, dominated by the growth of P shears during continued displacement.
(3) A fault linkage stage, in which low-angle Y shears coalesce to form a continuous fault surface parallel to the PDZ.

Compared with model 1, the thinner homogeneous configuration promotes earlier linkage of shear fractures, suggesting that layer thickness influences the efficiency of fault localization under strike–slip deformation.

5.3. Mechanically layered model (model 3)

Model 3 was designed to investigate the influence of mechanical stratification on strike–slip fault development. Quartz sand was used in both layers, with the upper layer composed of wet sand (water-to-sand volume ratio of 1:100) and the lower layer

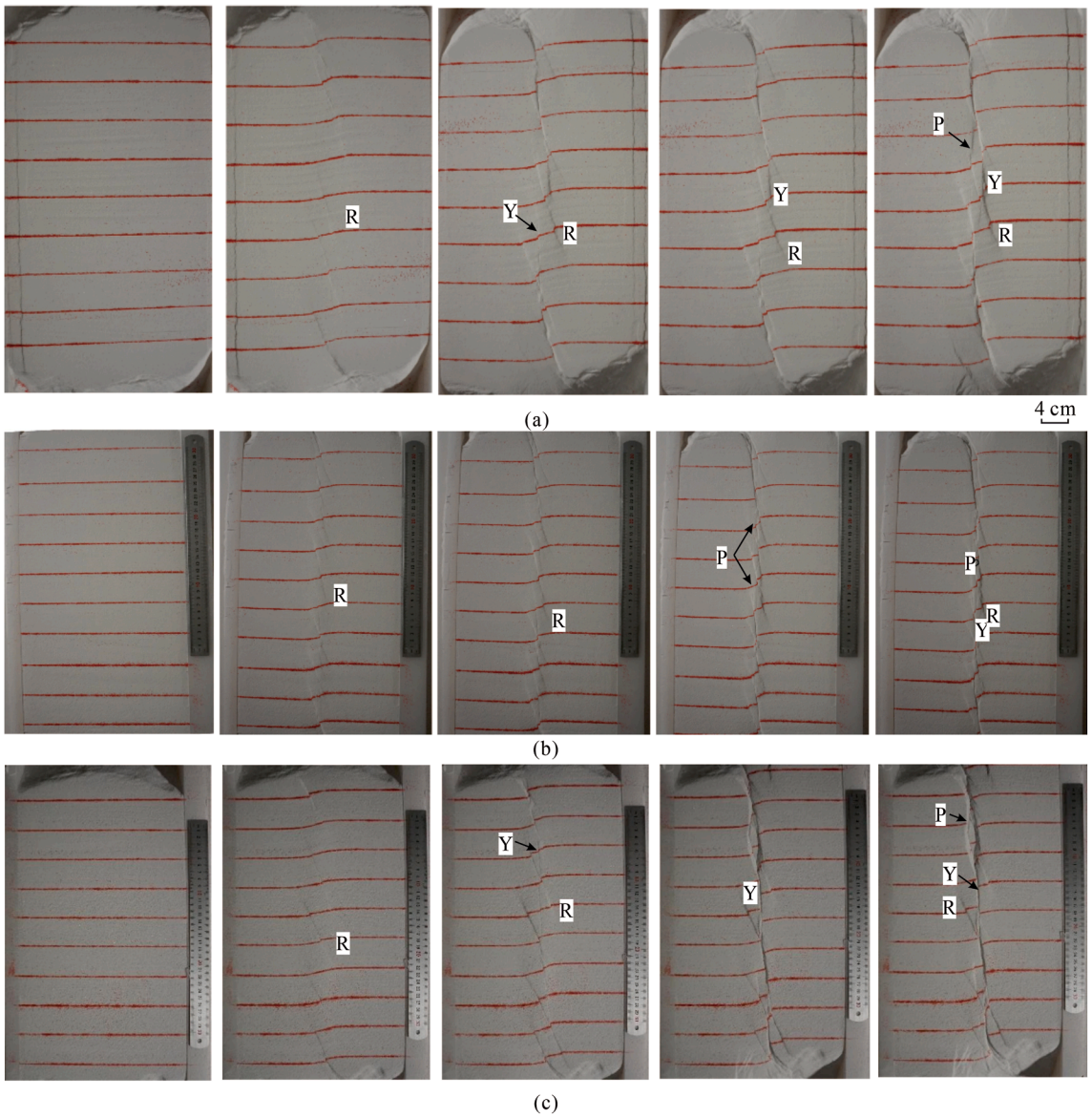

Fig. 5. Results of analog modeling experiments for three types of Riedel shear deformation: (a) thick dry sand model; (b) thin dry sand model; (c) upper wet sand, lower dry sand model.

composed of dry sand. Each layer was 3 cm thick, yielding a total model thickness of 6 cm, subdivided into 1.5 cm layers. In this configuration, wet sand represents relatively competent layers, whereas dry sand represents relatively weaker layers. Model dimensions were 50 cm in length and 24.5 cm in width, and deformation was imposed by single-sided left-lateral shear with displacement increments of 3.2 mm, 8.1 mm, 12.5 mm, and 20.1 mm.

The structural evolution of this model can be divided into three stages as Fig. 5(c).

(1) Distributed *R* shear initiation, with echelon *R* shears developing preferentially during early deformation.
(2) Y shear development stage, where Y shears nucleate at R shear step-overs and locally offset earlier R fractures.
(3) Fault zone maturation stage, in which Y shears subparallel to the PDZ progressively link to form a mature strike–slip fault zone.

Compared with homogeneous models, the mechanically layered configuration produces stronger vertical partitioning of deformation and delayed fault linkage, highlighting the important role of mechanical stratigraphy in controlling vertical segmentation and fault connectivity.

5.4. Implications for strike–slip fault architecture

Collectively, these physical modeling experiments demonstrate that strike–slip fault systems evolve through systematic stages of distributed shear, secondary fracture development, and progressive fault linkage. Variations in layer thickness and mechanical stratification exert a strong control on fault segmentation style, vertical connectivity, and the degree of fault zone organization. These experimental observations provide qualitative constraints on the structural architectures interpreted from seismic data in the Fuman Oilfield and support the inference that laterally continuous, well-linked fault systems correspond to higher cumulative

deformation and stronger slip intensity. Importantly, slip intensity in this study is evaluated using seismic-derived fault-zone geometry and displacement characteristics, while physical modeling serves to clarify the underlying deformation mechanisms and growth styles.

6. Discussion

6.1. Slip intensity and its control on reservoir effectiveness

Pronounced heterogeneity in reservoir effectiveness across the strike-slip fault zones of the Fuman Oilfield is fundamentally governed by variations in slip intensity, which integrates the cumulative kinematic history of fault activity and its associated deformation architecture. A representative comparison between the F_I12 and F_I17 fault zones reveals a striking production contrast: average single-well oil and oil-equivalent outputs in F_I12 are approximately 61,000 t and 69,000 t, respectively, whereas F_I17 reaches 275,000 t and 421,000 t. Such differences directly reflect first-order contrasts in reservoir scale, fracture connectivity, and the degree of tectono-diagenetic modification induced by long-term strike-slip deformation.

To quantitatively evaluate slip intensity and its reservoir implications, a multi-step analytical workflow was established to ensure methodological rigor and reproducibility. First, fault-zone widths were extracted from 31 wells intersecting the F_I12 and F_I17 fault zones using standardized seismic–well integration procedures (Figs. 6 and 7; Table 1). The F_I17 fault zone exhibits deformation-band widths ranging from 403 to 1591 m, with an average of 748 m, significantly exceeding the 269.6–706 m range (average 464 m) observed in F_I12. To minimize observational bias, each width measurement was independently constrained by: (1) seismic amplitude variation boundaries; (2) fault-parallel coherence anomalies, and (3) available borehole image logs, ensuring internal consistency across datasets.

Given the well-established logarithmic relationship between fault-zone width and cumulative slip, the substantially broader deformation belt developed along F_I17 indicates a markedly higher slip intensity relative to F_I12. This interpretation is further reinforced by high-resolution seismic geomorphological analysis. Structural relief values derived from 100 profiles across F_I17 range from −209 to +186 m, whereas 40 profiles across F_I12 show relief amplitudes of only 0–39 m (Fig. 8; Table 1). The large magnitude and bidirectional polarity of relief variations in F_I17 reflect repeated transpressional uplift and localized pull-apart subsidence, characteristic of fault zones that have experienced strong, long-lived, and episodic strike-slip reactivation. Such features are diagnostic of high slip intensity in mature strike-slip systems.

Uncertainty analysis indicates that these observations are robust. Horizon-picking uncertainty is estimated at ±10–15 m based on seismic frequency bandwidth and well–seismic tie quality, while fault-zone width uncertainty is ±20–35 m constrained by vertical resolution limits. These uncertainties are minor relative to the observed deformation magnitudes and do not affect the comparative interpretation between F_I12 and F_I17.

To further substantiate the mechanical–reservoir linkage, correlation analyses were conducted between slip-intensity-related parameters—namely (1) fault-zone width and (2) structural relief—and single-well production performance across both fault zones. Results demonstrate a statistically significant positive correlation between fault-zone width and structural relief ($R^2 = 0.68$, $n = 71$), as well as moderate to strong correlations between slip-intensity proxies and well productivity (fault-zone width: $R^2 = 0.61$; structural relief: $R^2 = 0.57$). Bootstrap resampling with 10,000 iterations confirms these relationships at the 95% confidence level, indicating that the observed trends are not artifacts of limited sample size or data heterogeneity.

Residual analysis further reveals no systematic bias between the two fault zones, implying that slip intensity, rather than local stratigraphic randomness or isolated lithologic effects, exerts the dominant control on productivity differentiation. From a geological perspective, higher slip intensity promotes wider fracture corridors, enhanced fracture connectivity, and greater effective reservoir volume through repeated deformation and fluid–rock interaction.

By integrating fault-zone width, structural relief, and production statistics, a clear and reproducible coupling is established between slip intensity, structural deformation scale, and reservoir effectiveness. Fault zones characterized by stronger cumulative strike-slip activity, such as F_I17, develop broader and better-connected fracture networks and higher-amplitude structural relief, thereby providing more favorable conditions for hydrocarbon accumulation and sustained production. Consequently, hierarchical differences in fault order and cumulative slip intensity between F_I12 and F_I17 represent the primary geological control on reservoir heterogeneity across the Fuman Oilfield.

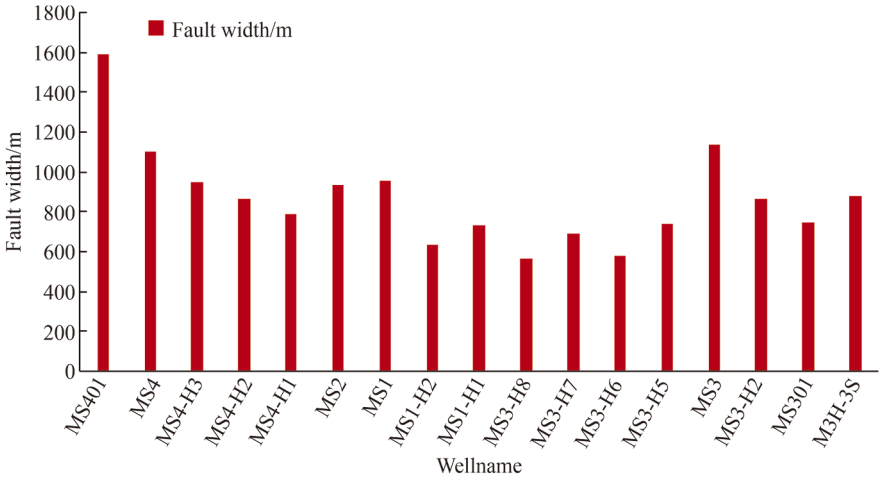

Fig. 6. Histogram of damage zone width at the well intersection points in the southern part of the F_I17 fault zone.

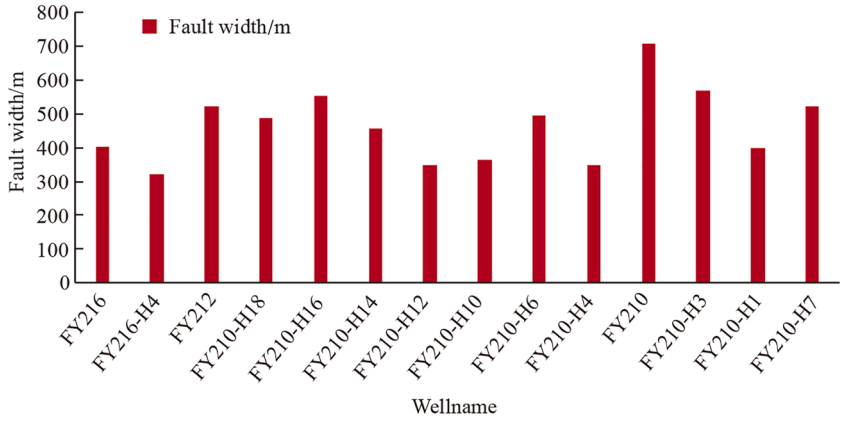

Fig. 7. Histogram of damage zone width at the well intersection points of the F_I12 fault zone.

Table 1
Comparison table of overall average single-well production and main controlling factors for the F_I12 and F_I17 fault zones.

Fault zone	Structural relief range (m)	Fault zone width range (m)	Average fault zone width (m)	Predicted avg. single-well oil production (10^4 t)	Predicted avg. single-well oil & gas equivalent (10^4 t)
F_I17 (Manshen 3–4 well area)	−209–186	403–1591	748	27.5	42.1
F_I12	0–39	269.6–706	464	6.1	6.9

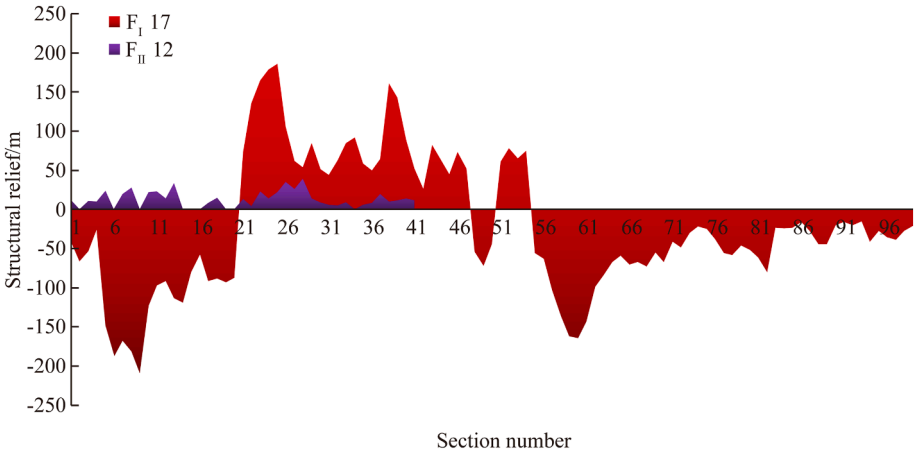

Fig. 8. Comparison chart of structural relief for the F_I17 and F_I12 fault zones.

6.2. Structural segmentation and its control on reservoir distribution

Segmented growth is a fundamental characteristic of strike-slip fault systems, and relay zones developed at segment boundaries commonly serve as key loci for strain localization, fluid migration, and hydrocarbon accumulation [27–29]. Based on integrated analyses of fault geometry, kinematics, and physical analog modeling, the Manshen 4–Manshen 3 fault zone is identified as comprising three genetically distinct structural segments: an extensional strike-slip duplex segment, a Riedel shear segment, and a horsetail extensional segment. These segments reflect different modes of secondary fault growth and linkage, and together define the along-strike heterogeneity of slip intensity within a single first-order fault zone.

Along the Manshen 4–Manshen 3 fault zone, the strike-slip system exhibits pronounced along-strike structural segmentation, which leads to significant variations in fault architecture and damage-zone development (Fig. 9). In the extensional strike-slip duplex segment, deformation is mainly accommodated by the overlap of two principal displacement zones together with numerous connecting secondary faults. The interaction of these structures produces a relatively wide and laterally continuous damage zone, reflecting locally intensified slip accumulation and distributed deformation.

In contrast, the Riedel shear segment is characterized by a typical R–P shear fracture system. In this structural configuration, large strike-slip damage zones preferentially develop at the step-over positions of synthetic R shears, whereas other portions of the segment remain comparatively weakly deformed. As a result, the overall fault architecture displays a braided structural pattern in plan view as Fig. 9(a), indicating strong spatial heterogeneity in deformation intensity along strike. A similar structural style is observed in the horsetail extensional segment, where large

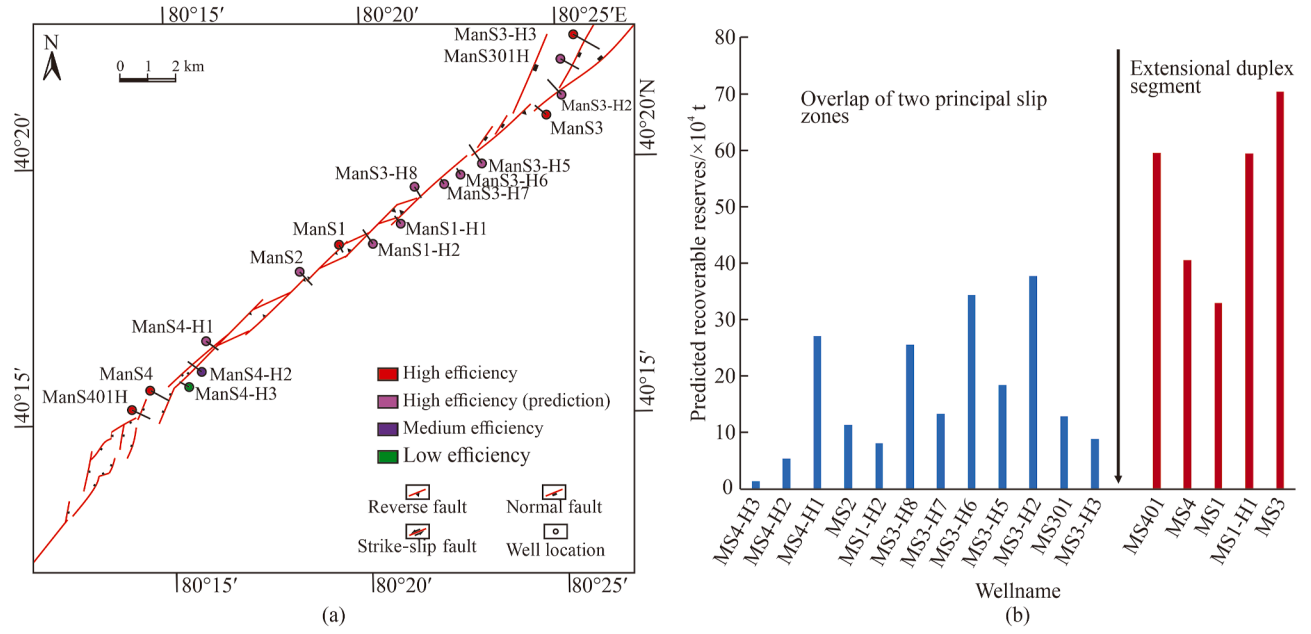

Fig. 9. Planar overlap of F_I17 and distribution map of single-well predicted recoverable reserves: (a) current single-well benefit classification map for the F_I17 fault zone (Manshen 3–4 well area) showing the distribution of high, high (prediction), medium, and low deficiency wells; (b) histogram of predicted single-well recoverable oil reserves for the Manshen 3-Manshen 4 well area, showing that the predict recoverable oil reserves in the extensional duplex are greater than that in the pop-up segment.

damage zones are mainly concentrated at closely spaced step-overs between the principal slip zone and branching faults, while more distal areas are characterized by relatively narrow deformation belts.

Statistical analysis of single-well recoverable oil reserves further demonstrates that this structural segmentation exerts a first-order control on reservoir distribution within the same fault zone. Wells located at lateral fault step-overs, where deformation and slip intensity are locally amplified, show an average damage-zone width of approximately 1.10 km and a predicted average single-well recoverable reserve of about 526,000 t. In contrast, wells drilled within non-step-over segments are associated with a significantly narrower average damage-zone width of approximately 0.77 km and a much lower predicted average recoverable reserve of about 170,000 t, see Fig. 9(b).

These results indicate that along-strike structural segmentation governs the spatial concentration of slip and deformation within the strike-slip fault system, which in turn controls fracture density, connectivity, and effective reservoir volume. Consequently, large-scale fault-controlled reservoirs preferentially develop near segment boundaries and relay zones where cumulative strike-slip deformation is maximized. This structural–reservoir coupling mechanism provides a geological explanation for the pronounced variability in single-well productivity observed along the Manshen 4–Manshen 3 fault zone and highlights the critical role of along-strike segmentation in predicting favorable reservoir development in strike-slip fault systems.

6.3. *Vertical stepped fault growth and its control on reservoir distribution*

In contrast to the F_I17 fault zone, which is dominated by lateral fault overlap, the F_I12 fault zone exhibits pronounced vertical stepwise linkage between secondary strike-slip faults within certain structural segments. These vertically stacked fault systems display different propagation heights, resulting in variable vertical overlap depths relative to the top of the target Yijianfang Formation. Such vertical segmentation represents an important dimension of slip-intensity expression in ultra-deep strike-slip systems.

Detailed seismic interpretation reveals that the depth of vertical overlap between secondary faults varies systematically along the F_I12 fault zone. For example, in the Fuyuan 212H well area, the overlap zone is located 741.8 m below the top of the Yijianfang Formation as Fig. 10(a), whereas in FY210–H18, FY210–H16, and FY210–H14, the corresponding depths are 606.1 m, 543.3 m, and 490.5 m, respectively, see Fig. 10(b)–(d). These variations reflect differences in vertical fault propagation and cumulative slip accommodation during fault growth.

Statistical analysis of predicted single-well recoverable reserves indicates a clear relationship between vertical step-over depth and production performance: wells associated with shallower vertical overlap zones exhibit significantly higher recoverable reserves (Fig. 11). Based on data from 13 wells in the Fuyuan 210 fault zone, a logarithmic relationship is identified between predicted recoverable reserves and the vertical distance from the fault overlap zone to the top of the Yijianfang Formation, expressed as $y = -113.5\ln(x) + 622.1$, with $R^2 = 0.8562$, indicating an excellent fit.

This relationship is interpreted in the context of a fault-controlled vertical hydrocarbon supply model. Hydrocarbons generated in the underlying Cambrian source rocks migrate upward preferentially along strike-slip fault zones. Within a single secondary fault, migration pathways are relatively efficient due to higher fracture connectivity. However, at vertical step-over zones between secondary faults, deformation is typically distributed within small-scale damage zones that have not yet evolved into fully connected fault cores. These zones may locally impede vertical hydrocarbon migration, reducing the volume of hydrocarbons reaching the overlying Yijianfang Formation.

The internal architecture of fault zones therefore plays a decisive role in controlling fluid flow. Well-connected fault segments facilitate efficient vertical migration, whereas structurally complex zones such as vertical step-overs may act as partial barriers or

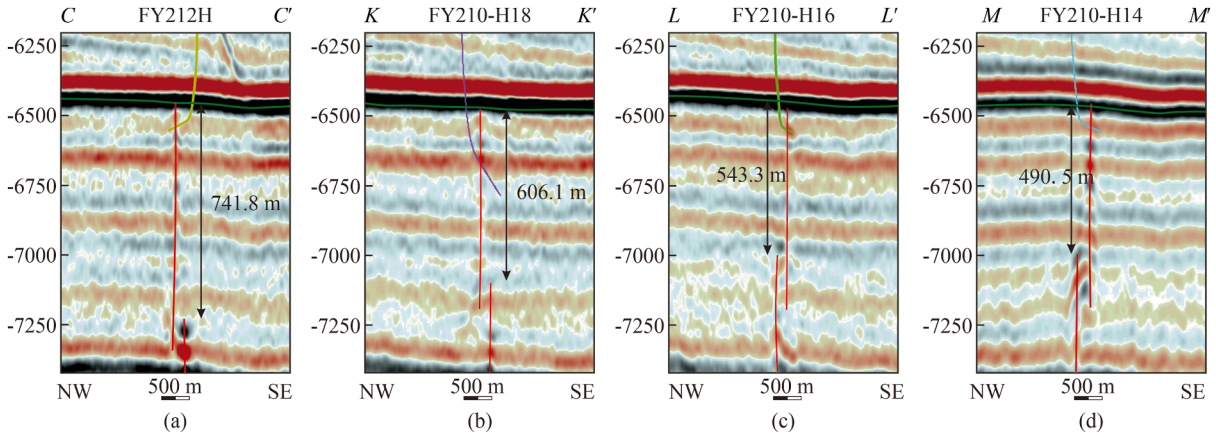

Fig. 10. Seismic profiles of typical wells in the F_I12 fault zone: (a) seismic cross-section along the FY212H well; (b) seismic cross-section along the FY210–H18; (c) seismic cross-section along the FY210–H16; (d) seismic cross-section along the FY210–H14.

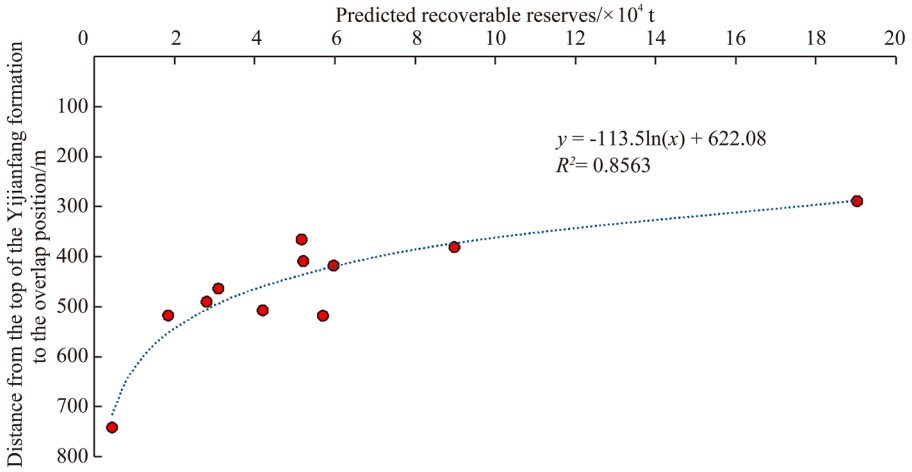

Fig. 11. Comparison chart of the relationship between single-well step-over situation and recoverable reserves in the Fuyuan 210 fault zone.

transient traps [12]. Accordingly, when the vertical overlap zone is located closer to the target reservoir, the hindrance effect occurs later in the migration pathway, allowing a greater volume of hydrocarbons to accumulate in the Yijianfang Formation. This explains the observed positive correlation between shallower vertical step-over depth and higher single-well productivity.

Overall, vertical stepped fault growth introduces a critical depth-dependent control on reservoir distribution in strike-slip fault systems characterized by “lower source–upper reservoir” configurations. Together with lateral segmentation, vertical fault linkage defines the three-dimensional heterogeneity of slip intensity and ultimately governs hydrocarbon accumulation efficiency in the F_I12 fault zone.

6.4. Integrated three-dimensional control of slip intensity on reservoir development

The results presented in sections 5.1–5.3 collectively demonstrate that slip intensity acts as a unifying parameter linking fault kinematics, structural architecture, and reservoir effectiveness in ultra-deep carbonate strike-slip systems. Rather than being expressed uniformly along a fault zone, slip intensity exhibits pronounced three-dimensional heterogeneity, manifested through variations in cumulative displacement magnitude (section 5.1), along-strike structural segmentation (section 5.2), and vertical fault linkage and propagation height (section 5.3).

At the fault-zone scale, higher slip intensity corresponds to wider damage zones, larger structural relief, and more persistent tectono-diagenetic modification, resulting in enhanced fracture connectivity and reservoir volume. Along strike, segmentation concentrates deformation at relay zones and step-overs, where localized amplification of slip intensity promotes the development of large-scale fracture corridors and high-productivity reservoirs. Vertically, differences in fault propagation height and step-over depth control the efficiency of upward hydrocarbon migration from deep Cambrian source rocks to Ordovician reservoirs, introducing a depth-dependent modulation of reservoir charging efficiency.

These three dimensions are not independent but mutually reinforcing. Zones characterized by strong cumulative slip, favorable lateral segmentation, and shallow vertical linkage represent optimal structural configurations for hydrocarbon accumulation. Conversely, areas with weaker slip intensity, poor fault connectivity, or deep vertical step-overs tend to form discontinuous or poorly charged reservoirs. This integrated three-dimensional framework explains the pronounced productivity contrasts observed both between the F_I12 and F_I17 fault zones and within individual fault systems.

From an exploration and development perspective, this study highlights that effective evaluation of ultra-deep strike-slip–controlled carbonate reservoirs requires moving beyond simple fault presence or length metrics. Instead, quantitative characterization of slip intensity and its three-dimensional structural expression provides a more robust basis for predicting reservoir distribution, ranking drilling targets, and reducing exploration risk in complex ultra-deep carbonate provinces.

7. Conclusions

Based on integrated drilling data, high-resolution seismic reflection interpretation, and structural analog modeling, this study systematically investigates the structural evolution and reservoir-controlling mechanisms of ultra-deep strike–slip fault zones in the Fuman area, Tarim Basin. The main conclusions are as follows:

(1) Ultra-deep strike–slip faults exhibit a combined growth pattern characterized by lateral segmentation and vertical stratification. Secondary shear faults progressively overlap and step in both horizontal and vertical directions, reflecting long-term multiphase reactivation under strong mechanical stratification of carbonate-dominated strata.
(2) Slip intensity is identified as the first-order control on the scale and effectiveness of fault-controlled reservoirs. Comparative analysis between the F_I12 and F_I17 fault zones demonstrates a clear positive relationship between cumulative slip intensity and reservoir scale. Fault zones with higher slip intensity develop wider damage zones, larger structural relief, and more persistent fracture connectivity, resulting in enhanced hydrocarbon accumulation and productivity.
(3) The lateral segmented growth of strike–slip faults governs the along-strike heterogeneity of fracture-controlled carbonate reservoirs. Slip intensity is preferentially concentrated at step-overs and relay zones of secondary shear faults, where wider damage zones and larger reservoir volumes are consistently developed.
(4) Vertical stepped fault growth exerts a critical control on hydrocarbon charging efficiency in reservoirs characterized by a lower-source–upper-reservoir configuration. Hydrocarbon productivity is positively correlated with the proximity of vertical fault step-overs to the target reservoir interval, with shallower overlap promoting more efficient upward hydrocarbon migration and higher hydrocarbon abundance.

Overall, this study establishes a reproducible semi-quantitative framework linking slip intensity, three-dimensional fault architecture, and reservoir effectiveness in ultra-deep carbonate strike–slip systems, providing a robust geological basis for reservoir prediction, drilling optimization, and exploration risk reduction in structurally complex ultra-deep carbonate provinces.

CRediT authorship contribution statement

Peng Cao: Methodology, Funding acquisition, Formal analysis, Conceptualization. **Xiongqi Pang:** Resources, Funding acquisition. **Jiajun Chen:** Writing – review & editing, Conceptualization. **Shaoying Chang:** Methodology, Investigation. **Jorge Costa Gomes:** Data curation.

Funding

This study was supported by the CNPC Scientific Research and Technology Development Project “Theory of Petroleum Systems and Accumulation Mechanisms of Unconventional Hydrocarbons” (No. 2021DJ0101), and the Joint Fund for Enterprise Innovation and Development of the National Natural Science Foundation of China (No. U19B6003-02).

Declaration of competing interest

The authors declare that they have no known competing financial interests or personal relationships that could have appeared to influence the work reported in this paper.

References

[1] Dengfa He, Chengzao Jia, Li Desheng, et al., The formation and evolution of the tarim multi-cyclical superimposed Basin, Petrol. Nat. Gas Geol. 26 (1) (2005) 64–77.
[2] J. Chen, D. He, F. Tian, et al., Control of mechanical stratigraphy on the stratified style of strike-slip faults in the central Tarim Craton, NW China, Tectonophysics 830 (2022) 229307.
[3] T. Hu, X. Pang, F. Jiang, Whole petroleum system theory and new directions for petroleum geology development, Adv. Geo-Energy Res. 11 (1) (2024) 1–5, https://doi.org/10.46690/ager.2024.01.01.
[4] Z. Jin, Hydrocarbon accumulation and resources evaluation: recent advances and current challenges, Adv. Geo-Energy Res. 8 (1) (2023) 1–4, https://doi.org/10.46690/ager.2023.04.01.
[5] X. Han, S. Deng, L. Tang, et al., Geometry, kinematics and displacement characteristics of strike-slip faults in the northern slope of Tazhong uplift in Tarim Basin: a study based on 3D seismic data, Mar. Petrol. Geol. 88 (2017) 410–427.
[6] S. Deng, H. Li, Z. Zhang, et al., Structural characterization of intracratonic strike-slip faults in the central Tarim Basin, AAPG (Am. Assoc. Pet. Geol.) Bull. 103 (1) (2019) 109–137.
[7] X. Han, L. Tang, S. Deng, et al., Spatial characteristics and controlling factors of the strike-slip fault zones in the Northern slope of Tazhong uplift, Tarim Basin: insight from 3D seismic data, Acta Geol. Sin. Engl. Ed. 94 (2) (2020) 516–529.
[8] T.P. Dooley, G. Schreurs, Analogue Modelling of Intraplate strike-slip Tectonics: a Review and New Experimental Results, Tectonophysics 574–575 (2012) 1–71.
[9] C. Chen, G. Ji, H. Wang, H. Huang, P. Baud, Q. Wu, Geology-engineering integration to improve drilling speed and safety in ultra-deep clastic reservoirs of the Qiulitage structural belt, Adv. Geo-Energy Res. 6 (4) (2022) 609–623, https://doi.org/10.46690/ager.2022.04.09.
[10] A.G. Sylvester, Strike-slip faults 100 (11) (1988) 1666–1703.
[11] Y.S. Kim, D.C.P. Peacock, D.J. Sanderson, Fault damage zones, J. Struct. Geol. 26 (3) (2004) 503–517.
[12] D.R. Faulkner, C.A.L. Jackson, R.J. Lunn, R.W. Schlische, Z.K. Shipton, C.A.J. Wibberley, M.O. Withjack, A review of recent developments concerning the structure, mechanics and fluid flow properties of fault zones, J. Struct. Geol. 32 (11) (2010) 1557–1575.
[13] J.S. Tchalenko, Similarities between shear zones of different magnitudes, Geol. Soc. Am. Bull. 81 (6) (1970) 1625–1640.
[14] Dengfa He, Li Desheng, The Taram Basin's Structural Evolution and Hydrocarbon Accumulation, Geological Publishing House, Beijing, 1996.
[15] Chengzao Jia, Wei Guoqi, Structural characteristics and hydrocarbon contamination of the tarim Basin, Sci. Bull. (Taipei) 47 (1) (2002) 1–8.
[16] Li Desheng, China multi-cyclonic Superimposed Hydrocarbon Basin Structural Studies, Science Press, Beijing, 2012.
[17] Jiaduo Liu, Lixin Qi, Tian Jingchun, et al., The Taram Basin: Structural Evolution and Sedimentary Framework, Science Press, Beijing, 2014.
[18] J. Wang, et al., Characteristics and genesis of shoal facies reservoir of the Lower Ordovician Tongzi Formation in southeastern Sichuan Basin, China, Adv. Geo-Energy Res. 7 (1) (2023) 1–12.
[19] Y. Li, et al., Development and evolution characteristics of strike-slip faults in Tarim Basin and its geological significance: a case study of FI17 Fault in Fumfn Oilfiefd, Adv. Geo-Energy Res. 7 (2) (2023) 156–168.
[20] L. Zhang, et al., Development characteristics and evolution model of FI19 Fault in Fumfn Oilfiefd, Tarim Basin, Adv. Geo-Energy Res. 7 (3) (2023) 210–222.
[21] M. Sun, et al., Characteristics of the hydrocarbon accumulation formed through the three structural cycles in Tarim Basin, Adv. Geo-Energy Res. 7 (4) (2023) 301–315.

[22] X. Chen, et al., Development characteristic and main controlling factors of the Ordovician karst caves in the Keping area, Tarim Basin, Adv. Geo-Energy Res. 8 (2) (2024) 123–135.
[23] Y. Wang, et al., Tectonic thermal evolution of Aksu area in the Tarim Basin, NW China: indications from apatite fission track thermochronology, Adv. Geo-Energy Res. 8 (3) (2024) 289–302.
[24] X. Deng, J. Chen, P. Cao, et al., Segmentation and lateral growth of intracratonic strike-slip faults in the northern Tarim Basin, NW China: influences on Ordovician fault-controlled carbonate reservoirs, Front. Earth Sci. 11 (2023).
[25] Huang Cheng, Characteristics and temporal sequence of small-scale strike-slip fault swash activity in the Tarim Basin: a case study of the Shunbei area, Petrol. Exp. Geol. 41 (2019) 379–389.
[26] M. Withjack, S. Callaway, Active normal faulting beneath a salt layer: an experimental Study of deformation patterns in the cover sequence 1, AAPG (Am. Assoc. Pet. Geol.) Bull. 84 (2000).
[27] D.C.P. Peacock, R.J. Knipe, D.J. Sanderson, Glossary of normal faults, J. Struct. Geol. 22 (3) (2000) 291–305.
[28] J.P. Evans, Thickness-displacement relationships for fault zones, J. Struct. Geol. 12 (8) (1990) 1061–1065.
[29] C. Brandes, D.C. Tanner, Chapter 2 - Fault Mechanics and earthquakes[M]// Tanner D, Brandes C. Understanding Faults, Elsevier, 2020, pp. 11–80.